ACS APPLIED MATERIALS & INTERFACES

www.acsami.org

Research Article

Growth of High-Quality Hexagonal Boron Nitride Single-Layer Films on Carburized Ni Substrates for Metal−Insulator−Metal Tunneling Devices

Yanwei He, Hao Tian, Protik Das, Zhenjun Cui, Pedro Pena, Ivan Chiang, Wenhao Shi, Long Xu, Yuan Li, Tianchen Yang, Miguel Isarraraz, Cengiz S. Ozkan, Mihrimah Ozkan, Roger K. Lake, and Jianlin Liu*

Cite This: *ACS Appl. Mater. Interfaces* 2020, 12, 35318−35327

Read Online

ACCESS | Metrics & More | Article Recommendations | Supporting Information

ABSTRACT: Two-dimensional (2D) hexagonal boron nitride (h-BN) plays a significant role in nanoscale electrical and optical devices because of its superior properties. However, the difficulties in the controllable growth of high-quality films hinder its applications. One of the crucial factors that influence the quality of the films obtained via epitaxy is the substrate property. Here, we report a study of 2D h-BN growth on carburized Ni substrates using molecular beam epitaxy. It was found that the carburization of Ni substrates with different surface orientations leads to different kinetics of h-BN growth. While the carburization of Ni(100) enhances the h-BN growth, the speed of the h-BN growth on carburized Ni(111) reduces. As-grown continuous single-layer h-BN films are used to fabricate Ni/h-BN/Ni metal−insulator−metal (MIM) devices, which demonstrate a high breakdown electric field of 12.9 MV/cm.

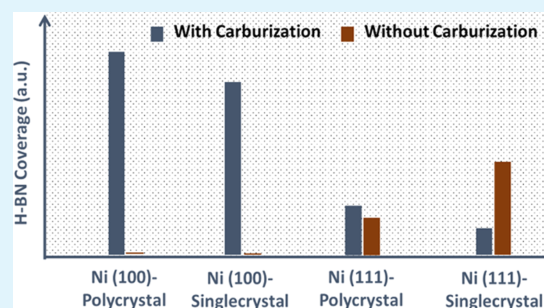

KEYWORDS: *hexagonal boron nitride (h-BN), molecular beam epitaxy (MBE), substrate engineering, two-dimensional (2D), electrical device*

Downloaded via UNIV OF CALIFORNIA RIVERSIDE on August 9, 2020 at 16:26:26 (UTC).
See https://pubs.acs.org/sharingguidelines for options on how to legitimately share published articles.

INTRODUCTION

The recent booming of two-dimensional (2D) materials has paved the way for the next generation of quantum electrical devices. For example, graphene with high electrical conductivity has been used as electrodes in nanodevices based on van der Waals materials such as capacitors;[1] 2D transition metal dichalcogenides (TMD) semiconductors such as MoS_2 are often used as the channel in field-effect transistors[2,3] and photodetectors.[4] Two-dimensional hexagonal boron nitride (h-BN) is a layered material isostructural to graphene. The replacement of carbon with alternating boron and nitrogen in the honeycomb-like sp^2 network creates an utterly different material with a wide band gap (5.9 eV),[5] high breakdown electric field,[6] high thermal conductivity,[7] and chemical inertness.[8] Due to these properties, h-BN has been used as an insulating layer in transistors[9] and capacitors,[10] a resistive switching layer for memristors,[11,12] an antiscattering substrate for graphene and MoS_2-based devices,[13−16] and so on. These applications impose a strict requirement on h-BN film quality and spark the exploration of synthesis methodologies to achieve better films.

The exfoliation method is a very common way to obtain high-quality 2D flakes for research purposes.[17] Even though many different types of exfoliation methods have been developed,[18−20] exfoliated flakes are usually very small in size. On the other hand, bottom-up synthesis methods such as chemical vapor deposition (CVD),[21] atomic layer deposition (ALD),[22,23] and molecular beam epitaxy (MBE)[24−31] can produce 2D h-BN films on wafer scale. The bottom-up synthesis of larger area films relies strongly on the catalytic effect of metal substrates. Various metal substrates have been used for h-BN growth, such as Fe,[32] Cu,[33,34] Co,[35,36] Ni,[37] etc. Because of their different properties, the thickness, uniformity, nucleation density, and growth speed of h-BN films are different. For example, Fe has been used for the precipitation growth of multilayer h-BN films thanks to its large nitrogen solubility,[38,39] while other metal substrates such as Cu and Ni have mostly been used for the growth of single-layer films. However, even though there are various metal substrates to choose from for h-BN growth, the pristine substrate cannot always yield desirable h-BN growth results. Engineering metal substrate properties by the incorporation of impurities provides a solution to this problem. For example, Si was

Received: April 19, 2020
Accepted: July 8, 2020
Published: July 8, 2020

© 2020 American Chemical Society

https://dx.doi.org/10.1021/acsami.0c07201
ACS Appl. Mater. Interfaces 2020, 12, 35318−35327

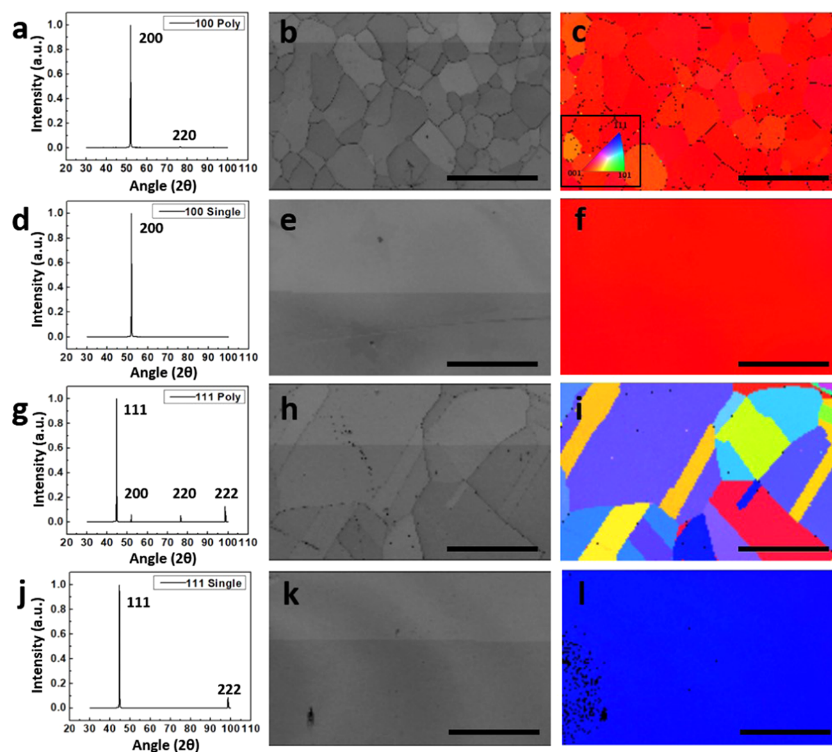

Figure 1. Characterization of four different types of Ni substrates. (a−c) (100)-dominated-polycrystal substrate; (d−f) (100)-single-crystal substrate; (g−i) (111)-dominated-polycrystal substrate; (j−l) (111)-single substrate. The first column (a), (d), (g), and (j) shows XRD results, the second column (b), (e), (h), and (k) shows EBSD band contrast maps, and the third column (c), (f), (i), and (l) shows EBSD IPF Z images taken at the same area shown in the second column. All scale bars here are 500 μm.

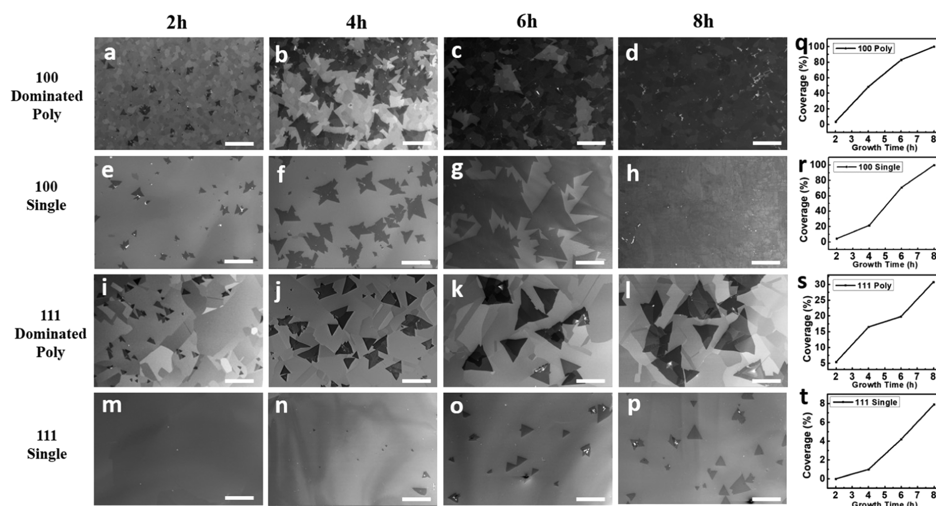

Figure 2. Results of time-dependent growth of h-BN on carburized Ni substrates. (a−d) SEM images of h-BN samples on (100)-dominated-polycrystal substrates at a growth time of 2, 4, 6, and 8 h, respectively, (e−h) SEM images of h-BN samples on (100)-single-crystal substrates at a growth time of 2, 4, 6, and 8 h, respectively, (i−l) SEM images of h-BN samples on (111)-dominated-polycrystal substrates at a growth time of 2, 4, 6, and 8 h, respectively, (m−p) SEM images of h-BN samples on (111)-single-crystal substrates at a growth time of 2, 4, 6, and 8 h, respectively. (q−t) Plots of h-BN coverage versus growth time on (100)-dominated-polycrystal, (100)-single-crystal, (111)-dominated-polycrystal, and (111)-single-crystal Ni substrates, respectively. All Ni substrates were carburized with 0.5 sccm C_2H_2 for 4 min at 900 °C before growth. All samples were grown at 880 °C with 10 sccm ammonia and B_2O_3 cell kept at 1150 °C. All scale bars here are 500 μm.

incorporated in Fe substrates to lower the nucleation density of h-BN for the growth of larger flakes;[40] oxygen was reported in improving the catalytic effect of Fe and Cu for better film growth;[41,42] and a recent article from our group reported that carburized Co substrates can improve the adsorption of B and N and eliminate the adlayer growth.[43]

In this work, we extend our study of the carburization effects on h-BN growth to Ni substrates. Four different kinds of Ni substrates were obtained after the thermal annealing process, namely, the (100)-polycrystal substrate, the (100)-single-crystal substrate, the (111)-dominated-polycrystal substrate, and the (111)-single-crystal substrate. Single-layer h-BN films with different morphologies were grown on these four types of

https://dx.doi.org/10.1021/acsami.0c07201
ACS Appl. Mater. Interfaces 2020, 12, 35318−35327

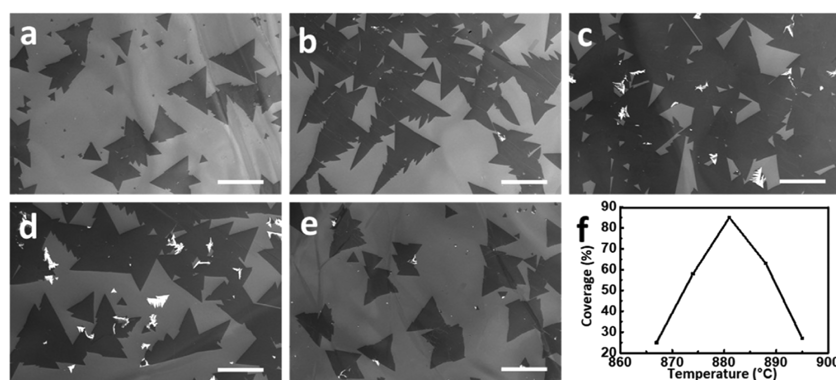

Figure 3. Temperature-dependent growth of h-BN on carburized Ni(100)-single-crystal substrates. (a−e) SEM images of as-grown h-BN samples with growth temperature ranging from 867 to 895 °C, respectively, (f) plot of h-BN coverage versus growth temperature for this batch of samples. All samples were grown with 10 sccm ammonia and B_2O_3 cell kept at 1150 °C for 6 h. All scale bars here are 500 μm.

substrates with and without carburization by MBE. The density functional theory (DFT) and climbing image nudged elastic band (CI-NEB) methods were employed to help explaining the results. Metal−insulator−metal (MIM) devices were fabricated to characterize their electrical properties, and a high breakdown electric field of 12.9 MV/cm was demonstrated for a single-layer h-BN film.

■ RESULTS AND DISCUSSION

Ni substrates evolve into four different textures after the thermal annealing process (Supporting Information, S1). Figure 1 presents the characterization results of the four different substrates, with the first column showing the X-ray diffraction (XRD) results, and the second and third columns showing the electron backscatter diffraction (EBSD) band contrast and *Z*-axis inverse pole figure (IPF Z) images, respectively. The XRD results reveal the dominating surface directions in a large area, while the EBSD results provide detailed information about the surface texture, such as grain size and high indexed surfaces. The substrates having results in Figure 1a−c, d−f, g−i, and j−l were designated as (100)-dominated-poly substrate, (100)-single-crystal substrate, (111)-dominated-polycrystal substrate, and (111)-single-crystal substrate, respectively. It is worth noting that even though the XRD result in Figure 1g shows a dominating (111) peak for (111)-dominated-polycrystal substrates, the corresponding IPF Z image in Figure 1i reveals that the (111) grains only occupy a small portion across the whole surface. As a matter of fact, the surface also contains (100) and many other high-index surfaces. This discrepancy is caused by the diffraction selection rules of XRD; for face-centered cubic (FCC) metal, only those surfaces with Miller indexes (h, k, and l) all odd or all even are allowed for reflections. On the other hand, even though EBSD is more detailed in showing surface textures, it can only show an image from a very small area of the whole sample. Therefore, both XRD and EBSD were used to obtain accurate information about the substrates.

Figure 2 shows scanning electron microscopy (SEM) characterization results of growth time-dependent samples on the four different types of substrates. All samples were grown at 880 °C with 10 sccm ammonia and B_2O_3 cell at 1150 °C. Before the introduction of B and N sources, the Ni substrates were carburized with 0.5 sccm C_2H_2 for 4 min at 900 °C. The C_2H_2 gas flow rate and duration were controlled to attain a small amount of interstitial carbon in the Ni substrate for tuning its catalytic strength only; in other words, the amount of carbon was not enough for the formation of any graphene, graphite, or carbide during growth. The proof of this using X-ray photoelectron spectroscopy (XPS) studies is given elsewhere[37,55] and later in the text. Similar studies of carburization of Co substrates showed that while high-amount carbon incorporation results in the formation of graphene or graphitic structures, low-amount carbon incorporation in the Co substrates as interstitials does not lead to these structures, instead it effectively tunes the catalytic effect of the substrates for h-BN growth.[25,35,43] Figure 2a−d and e−h show SEM images of h-BN films on (100)-dominated-polycrystal and (100)-single crystal substrates, respectively. The growth results on these (100)-substrates are similar. Small and sparse h-BN flakes are formed at the early growth stage, and these flakes grow larger and merge with each other as the growth time increases. Continuous films are formed after 8 h. The growth rate of h-BN on the polycrystalline substrates is slightly larger than that of the single-crystal substrates, which may be due to an increase in the nucleation rate of h-BN around the grain boundaries.[44] In addition, the h-BN film on the (100)-dominated-polycrystal substrate appears to be less uniform due to the formation of adlayers (white features in Figure 2d), which is also attributed to crystallographic defects on the polycrystal substrate.[44] Figure 2i−l shows SEM images of h-BN films on (111)-dominated-polycrystal substrates. The growth results for growth times less than 4 h are similar to that of the (100) substrates. However, as the growth time increases further, the flakes grow larger, but they do not merge to form continuous films. Instead, sub-millimeter-sized triangular flakes are formed after 8 h growth. Figure 2m−p shows SEM images of h-BN samples on (111)-single-crystal substrates. Intriguingly, even though the Ni(111) surface has the same 6-fold symmetry as that of h-BN, the coverage and flake size of h-BN are extremely small compared to the growth on all other three substrates, indicating that Ni(111)-single-crystal surfaces are less preferable for h-BN growth under the growth conditions imposed. In contrast, larger h-BN flakes and higher coverage of h-BN on (111)-dominated-polycrystal substrates clearly indicate that the nucleation and growth have been assisted by other factors such as grain boundaries and existing various other facets such as (100) and high indexed surfaces (Figure 1g,i), which may be more preferable nucleation surfaces than (111).[45,46] Figure 2q−t show the plots of h-BN coverage as a function of growth time for the samples

https://dx.doi.org/10.1021/acsami.0c07201
ACS Appl. Mater. Interfaces 2020, 12, 35318−35327

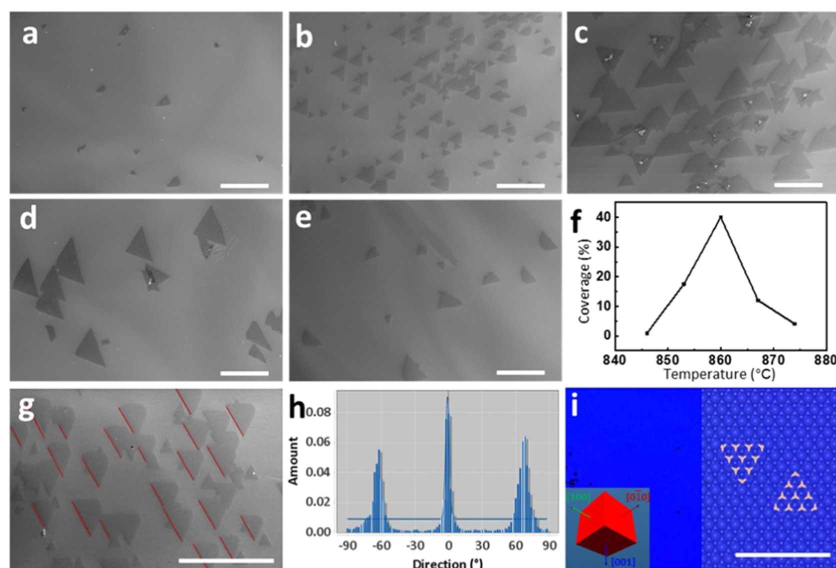

Figure 4. Temperature-dependent growth of h-BN on pristine Ni(111)-single-crystal substrate. (a−e) SEM images of as-grown h-BN samples with growth temperature ranging from 846 to 874 °C, respectively, (f) plot of h-BN coverage versus growth temperature for this batch of samples, (g) SEM image of another area on sample shown in (b) for EBSD mapping. The red lines mark one of the dominant edge directions, (h) directionality histograms of image (g) showing three dominated edge directions separated by 60°, (i) IPF Z image of EBSD mapping showing the blue color of (111) surface. Inset on the lower left shows the corresponding unit cell. Transparent inset on the right-hand side shows the substrate atom arrangement revealed by the unit cell. Two equivalent h-BN flakes with B atoms are sitting on FCC sites, and N atoms sitting on top sites. All samples were grown with 10 sccm ammonia and B_2O_3 cell kept at 1150 °C for 6 h. All scale bars here are 500 μm.

grown on (100)-dominated-polycrystal, (100)-single-crystal, (111)-dominated-polycrystal, and (111)-single-crystal Ni substrates, respectively. The coverage data were obtained using the ImageJ software package.[43] While the coverage increases with the increase of the growth time on all four types of substrates, the growth speed decreases monotonously for the h-BN on the substrates from (100)-dominated-polycrystal, to (100)-single-crystal, to (111)-dominated-polycrystal, and to (111)-single-crystal Ni substrates.

The (100)-single-crystal and (111)-single-crystal Ni substrates were selected for temperature-dependent growth to further study h-BN growth behavior. All samples were grown with 10 sccm ammonia and B_2O_3 cell at 1150 °C for 6 h. Figure 3a−e shows SEM images of h-BN samples on carburized single-crystal Ni(100) substrates at a growth temperature ranging from 867 to 895 °C, respectively. Figure 3f shows the evolution of h-BN coverage versus growth temperature for this batch of samples. The h-BN coverage increases as the substrate temperature increases, the highest coverage of 85% is attained at around 880 °C, and the coverage decreases as the temperature increases further. Figure 4a−e shows SEM images of h-BN samples on single-crystal Ni(111) substrates without carburization at a growth temperature from 846 to 874 °C, respectively. The evolution of h-BN coverage versus growth temperature is plotted in Figure 4f. Similarly, the h-BN coverage increases as the substrate temperature increases. The peak coverage is achieved at around 860 °C, which is about 20 °C lower than that on single-crystal Ni(100) substrates. As the substrate temperature increases beyond 860 °C, the coverage decreases. These coverage−temperature plots indicate that the growth speed of h-BN has a nearly parabolic relationship with the growth temperature. This phenomenon was also reported in the MBE growth of GaAs.[47,48] In general, there is an optimized growth temperature, around which the adsorption, diffusion, and bonding processes coordinate with each other to achieve the highest growth speed. Decreasing the temperature will hinder the diffusion and bonding processes, while increasing the temperature will enhance desorption exponentially. Therefore, both lead to a lower growth rate. Another interesting phenomenon is that most of the flakes are well aligned on the (111)-single-crystal substrates. Figure 4g shows an SEM image, which was taken from another part of the sample shown in Figure 4b. One of the aligned edges is marked with red lines to illustrate the alignment. The edge directions of the h-BN flakes were further analyzed with ImageJ software.[49] Figure 4h shows the result. Three groups of edge's directions are observed with the center separated by around 60°. Figure 4i shows the result of EBSD mapping of the same area shown in Figure 4g. The blue color in IPF Z images represents (111) surfaces, while the corresponding unit cell reveals the close-packed directions of surface atoms. Based on the surface direction revealed by unit cell, we can tell that red lines in Figure 4g are aligned with the $\langle 10\bar{1} \rangle$ direction. An image of the corresponding Ni atom arrangement is superimposed on the IPF Z figure. Based on the SEM and EBSD results, two atom models of h-BN flake with identical registration relationship to the substrate are overlaid on the IPF Z figure, with B siting on the FCC site, and N siting on the TOP site. This registration relationship of h-BN on the Ni(111) surface is supported by the DFT calculation shown in Figure S1 in the supporting information. The same conclusion was drawn from experimental[50,51] and DFT calculation results reported elsewhere.[52−54] The work here suggests that Ni(111) substrates can be another candidate for wafer-scale single-crystal h-BN film growth. Nevertheless, the peak coverage is only about 40% under this growth condition. Increasing the growth time should lead to the full coverage.

To reveal the effect of carburization on the four types of substrates for h-BN growth, we compare results in Figure 5. The first and the second columns show SEM images of the

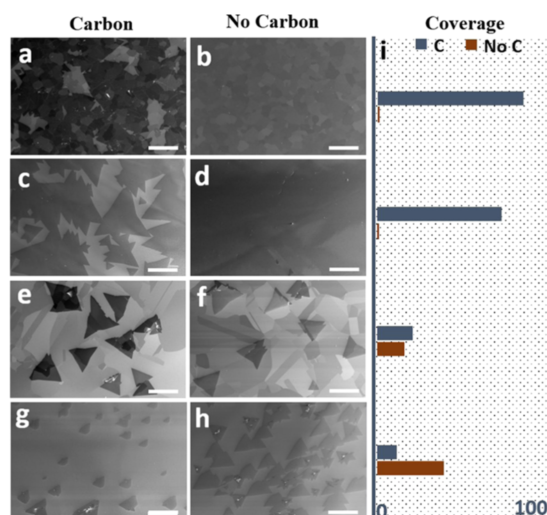

Figure 5. Carburization-dependent growth of h-BN on different Ni substrates. (a, b) SEM images of h-BN samples on (100)-dominated-polycrystal substrates with and without carburization, respectively, (c, d) SEM images of h-BN samples on (100)-single-crystal substrates with and without carburization, respectively, (e, f) SEM images of h-BN samples on (111)-dominated-polycrystal substrates with and without carburization, respectively, (g, h) SEM images of h-BN samples on (111)-single-crystal substrates with and without carburization, respectively, (i) comparison of h-BN coverage with and without carbon on each substrate. All samples were grown with 10 sccm ammonia and B_2O_3 cell kept at 1150 °C for 6 h. Carburization was done by introducing 4 sccm C_2H_2 for 4 min at 900 °C prior to growth. All scale bars here are 500 μm.

samples grown on carburized substrates and pristine substrates, respectively. The third column shows the comparison of h-BN coverage for each type of substrates. Figure 5a,c,e shows the 6 h growth samples reproduced from Figure 2. The results on (111)-single-crystal substrates (Figure 5g,h) were obtained at a growth temperature of 860 °C, namely 20 °C lower than that for other samples. All other growth conditions are the same. Figure 5a/b,c/d shows SEM images of h-BN samples on (100)-polycrystal and (100)-single-crystal Ni substrates, respectively. Substantial coverage of h-BN was obtained on carburized substrates, but no growth occurred on pristine substrates, which means that the carburization is essential for h-BN growth on Ni(100) surfaces at current growth conditions. Details regarding this aspect have already been reported elsewhere.[55] Figure 5e/f,g/h shows SEM images of h-BN samples grown on (111)-dominated-polycrystal and (111)-single-crystal Ni substrates, respectively. There is growth on both carburized and pristine substrates: h-BN coverage is slightly higher on the carburized (111)-dominated-polycrystal substrate than that on the pristine (111)-dominated-polycrystal substrate. Since the (111)-dominated substrates consist of the mixture of (111), (100), and some other high indexed grains as shown in Figure 1, the incorporation of carbon into (100) and other higher-index surfaces might have catalyzed more growth on the substrates. On the other hand, the h-BN coverage is clearly smaller with carburization than without carburization on (111)-single-crystal Ni substrates. This is intriguing since the incorporation of carbon in pure Ni(111) substrates reduces its catalytic effect, which is exactly opposite to our observations on Ni(100) substrates.[55]

To clarify the effect of carbon incorporation in Ni(111) on the nucleation and growth of h-BN, we carried out simulations using DFT and CI-NEB methods. Detailed information about the methodologies are reported elsewhere[55] and also briefly summarized in the Methods Section. Since ammonia and B_2O_3 were used as sources, various species such as B and N atoms, B_xO_y, NH_x chemical compounds may be present on the hot Ni substrates during the growth. Nevertheless, Ni was used as a catalyst for N adatom and H_2 generation from the decomposition of NH_3,[56] and B_2O_3 is thermally decomposed to B atoms and O_2 gas in the effusion cell at high temperature. Thus, B and N atoms are considered as the dominant reactive species on the substrates for the nucleation and growth of h-BN here. The nucleation activation energy E_a is expressed as

$$E_a = E_{ads} + E_{diff} + E_{att} \quad (1)$$

where E_{ads} is the adsorption energy, E_{diff} is the energy barrier for diffusion on the substrate surface, and E_{att} is the attachment energy, namely, the energy barrier to form a B−N covalent bond. Smaller E_a means easier growth, in turn, larger film coverage. Since the amount of carbon incorporation in Ni(111) is low, the change to the lattice constant of Ni(111) can be negligible, which means that the change of attachment energies before and after carburization can be assumed to be insignificant. Thus, the effect of carburization on the nucleation is mainly dominated by the absorption and diffusion energies. The adsorption energies of B and N atoms on Ni are defined in the following expression

$$E_{ads} = -E_{B/N} - E_{surface} + E_{B/N\ on\ surface} \quad (2)$$

where $E_{B/N}$ is the chemical potential of B or N, $E_{surface}$ is the energy of the clean Ni surface without adsorbents, and $E_{B/N\ on\ surface}$ is the total energy of B and N adsorbed on the Ni surface. Smaller E_{ads} means more stable adsorption. Three different adsorption sites were calculated, namely, the FCC site, the HCP site, and the Top site. Figure 6a shows the DFT calculation results of adsorption energy. The adsorption energies of B and N atoms on the Ni(111) surface are larger with a carbon atom placed at the adjacent subsurface octahedral site, indicating the adverse effect of embedded

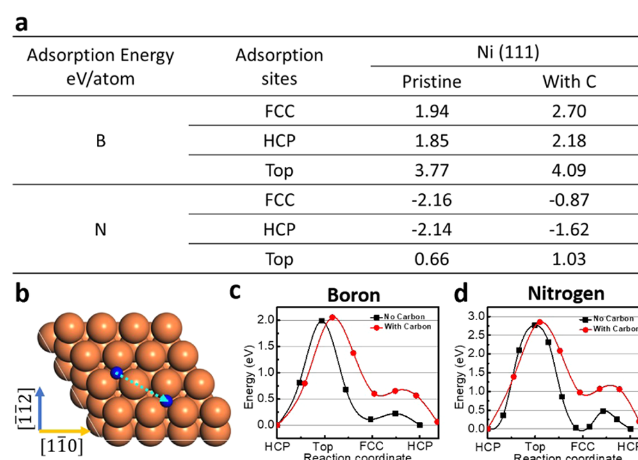
a

Adsorption Energy eV/atom	Adsorption sites	Ni (111)	
		Pristine	With C
B	FCC	1.94	2.70
	HCP	1.85	2.18
	Top	3.77	4.09
N	FCC	-2.16	-0.87
	HCP	-2.14	-1.62
	Top	0.66	1.03

Figure 6. Theoretical calculation of adsorption and diffusion energies of B and N atoms on Ni(111) with and without an embedded interstitial carbon at the adjacent subsurface octahedral site. (a) DFT calculation of adsorption energies of B and N on Ni(111), (b−d) CI-NEB calculation of diffusion energy of B and N on Ni(111). (b) Top view of the diffusion path from an FCC site to an adjacent HCP site; (c, d) are the energy profiles of B and N diffusing along the path indicated in (b).

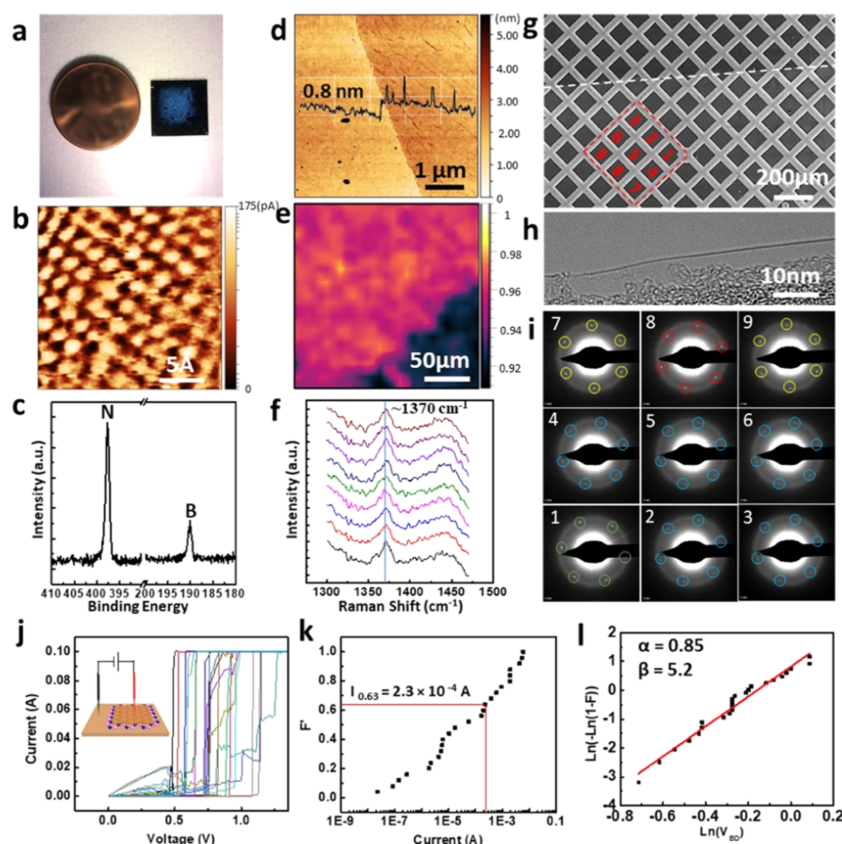

Figure 7. In-depth characterization of the continuous h-BN film grown on the (100)-single-crystal Ni substrate. (a) Photo of as-grown h-BN samples placed next to a penny coin. The blue color is caused by Ni surface reconstruction under the h-BN film, (b) STM image of the as-grown h-BN film showing the honeycomb structure of a single-layer film, (c) XPS spectrum of the as-grown h-BN film, (d) AFM image of a transferred h-BN film, with the inset showing a film thickness of 0.8 nm, (e) Raman mapping of the transferred h-BN film, (f) nine Raman spectra obtained from nine random positions on Raman mapping showing the peak position at around 1370 cm^{-1}, (g) SEM image of the h-BN film transferred onto a transmission electron microscopy (TEM) grid. The dotted line highlights the boundary of the h-BN film, and the red square and numbers mark the position of taking selected-area electron diffraction (SAED) patterns, (h) TEM image taken at the edge of the h-BN film, (i) nine SAED patterns taken at corresponding areas marked in (g). The colored circles mark SAED patterns with the same azimuthal angles, (j) current−voltage characteristics of 25 Ni/h-BN/Ni capacitor devices. The inset shows the schematic of the device, (k) cumulative probability distribution of tunneling current at 0.1 V, and (l) Weibull plot of breakdown voltages.

carbon on the adsorption process. Figure 6b−d shows the CI-NEB calculation of diffusion energy. The diffusion path is shown in Figure 6b. A B, or N atom diffuses from an HCP site, through a TOP site, an FCC site, and a bridge site to the second nearest HCP site, so that all diffusion scenarios are included. Figure 6c,d show the calculated energy profiles of B and N versus adsorption positions. The black lines are energy profiles on pristine substrates, and the red lines are energy profiles on substrates with a carbon placed at the octahedral site along the diffusion path. As seen from Figure 6c,d, the energy barriers of B and N diffusing from an HCP site to the second nearest HCP site are increased on the carburized substrate, indicating the adverse effect of carbon incorporation on the diffusion process. With the increased adsorption and diffusion energies, the h-BN nucleation energy E_a increases with the incorporation of carbon, which reduces the h-BN growth on Ni(111) surfaces. The conclusion is consistent with our experimental results.

Finally, we carried out the in-depth characterization of the continuous h-BN film on carburized Ni(100)-single-crystal substrate (Figure 2h) since the film arguably has the best uniformity and continuity among all samples studied here. Figure 7a shows a photo of an as-grown sample placed next to a penny. The area covered by the h-BN film exhibits blue color under the illumination of white light from a certain angle. The blue color is a result of light scattering from the reconstructed surface, which is studied in detail in the Supporting Information, S3. Figure 7b shows a scanning tunneling microscopy (STM) image of the sample. The image was taken using a Nanosurf tabletop STM system at room temperature and an ambient environment. Positive voltage was applied to the tip; therefore, only the N atom was resolved. The image is distorted slightly due to the thermal drift, but the hexagonal arrangement of N atoms is evident. The average distance of N atoms was measured to be 0.24 nm, which is close to its theoretical value of 0.25 nm. Figure 7c shows the XPS spectrum of the sample. B_1s and N_1s peaks are located at around 190 and 397.5 eV, respectively. The multipeak fitting of XPS data is shown in the Supporting Information, S4, indicating the existence of 2D h-BN without graphene, carbide, or other species. Figure 7d shows the atomic force microscopy (AFM) results taken on a transferred h-BN film. The thickness was measured to be 0.8 nm, corresponding to the single-layer h-BN film. The larger experimental value comparing to the theoretical value is due to the tip effect and trapped water and gas molecules in the interface between the h-BN and the SiO_2

https://dx.doi.org/10.1021/acsami.0c07201
ACS Appl. Mater. Interfaces 2020, 12, 35318−35327

substrate.[44] Figure 7e shows the Raman mapping near the edge of the transferred h-BN film, indicating uniform contrast over 200 μm^2. Figure 7f shows nine Raman spectra extracted randomly from the region with rose color on the mapping data. The peak position is determined to be 1370 cm^{-1}, which implies that the h-BN film is single-layer.[57]

Figure 7g shows an SEM image of the h-BN film transferred on a TEM grid. The lower half is covered by the h-BN film, and the white line marks the edge of the h-BN film. The red square and numbers mark the region for selected-area electron diffraction (SAED) analysis. Figure 7h shows a TEM image taken at the edge of the h-BN film where the film is folded, enabling the imaging of the cross section of the film. A single-layer h-BN film is revealed. Figure 7i shows the nine SAED patterns. The dimension of the square meshes marked in Figure 7g is 200 μm, and the SAED patterns were taken at their center areas. SAED patterns with the same azimuth angle were marked with the same color. Identical azimuth angles indicate identical atom arrangement; thereby, these atoms in the investigated area belong to the same crystal domain. As seen from the figure, three sets of SAED patterns are observed, indicating the polycrystal nature of the h-BN film. Even though the substrate is single-crystal Ni(100), the h-BN flakes grown on top are randomly oriented due to the lack of epitaxial relationship, leading to polycrystal films. The grain size of the polycrystal h-BN film is around 600 μm based on the SEM and TEM results. Larger grain size yields fewer grain boundaries.

Figure 7j shows $I-V$ characteristics of 25 metal–insulator–metal (MIM) devices. The fabrication and characterization methodology are described in the Methods Section. The inset is the characterization configuration. The voltage is swept from 0 to 1.5 V, and the compliance current is set to be 0.1 A. At low voltages (<0.2–0.3 V), the current mostly increases linearly with an increase of the voltage, indicating direct tunneling.[58] The tunneling current fluctuates in some devices as the voltage increases, which is due to the trap-assisted tunneling.[59] These traps are formed due to the defects, such as h-BN grain boundaries, as discussed above. As the voltage is further increased, the devices start to breakdown and the current increases sharply and reaches the compliance current. Figure 7k shows the cumulative probability of the tunneling currents at a bias of 0.1 V. The most probable tunneling currents at 0.1 V are obtained by setting the cumulative probability at 63.2%, yielding a value of 2.3×10^{-4} A. The direct tunneling current of an MIM device is expressed as[58,60,61]

$$I(V, T) = I(V, 0) \times \left\{1 + \left[\frac{3 \times 10^{-9}(dT)^2}{\Phi_B/q}\right]\right\} \quad (3)$$

where $I(V, 0) = \frac{A_{eff}\sqrt{2m_B}q^2V}{h^2d}\exp\left(\frac{-4\pi d\sqrt{2m_B}}{h}\right)$, m is the electron effective mass, which is 0.26 m_0, h is Plank's constant, q is the fundamental charge, Φ_B is 3.0 eV,[10,61,62] d is 0.66 nm assuming that this is the van der Waals distance between the top and the bottom contacts, and T is equal to 293 K. Based on the tunneling current value at 0.1 V, an effective area A_{eff} is calculated to be 0.027 μm^2. This value is orders of magnitude smaller than the physical device area of 50 μm × 50 μm, suggesting that electron tunneling goes through a very small local area only.[61] Our AFM analysis (Supporting Information, Figure S3) reveals that the surface of as-grown films is corrugated due to metal surface reconstruction, which may lead to gaps between the h-BN film and the bottom Ni electrode, thus results in a small effective area. Figure 7i shows the Weibull plot of breakdown voltage V_{BD}. The cumulative failure probability F of breakdown voltage is defined as[61,63]

$$F(V_{BD}) = 1 - \exp\left[-\left(\frac{V_{BD}}{\alpha}\right)^{\beta}\right] \quad (4)$$

where the scale parameter α indicates the most probable breakdown voltage and the shape parameter β indicates the width of the distribution. This function can also be rearranged as

$$\ln[-\ln(1 - F)] = \beta \ln(V_{BD}) - \beta \ln \alpha \quad (5)$$

Therefore, based on the plot of $\ln[-\ln(1 - F)]$ versus $\ln(V_{BD})$, we extracted the value of α and β as 0.85 and 5.2, respectively. Using the breakdown voltage indicated by α, 0.85 V, we can derive the breakdown electric field of the single-layer h-BN film as 12.9 MV/cm, which is comparable to that of exfoliated h-BN.[6]

CONCLUSIONS

We have presented the results of h-BN growth on four different kinds of Ni substrates. It has been found that carburization can enhance h-BN growth on Ni(100) surfaces while suppresses h-BN growth on Ni(111) surfaces. DFT and CI-NEB calculations reveal that the adsorption and diffusion of B and N atoms on Ni(111) are suppressed by embedded interstitial carbon atoms. Well-aligned h-BN flakes can be obtained on Ni(111) substrates. MIM devices were fabricated on the as-grown single-layer h-BN film on single-crystal Ni(100), and the breakdown electric field was determined to be 12.9 MV/cm. Our work reveals the strong influence of substrate properties on h-BN growth and explores the strategy of engineering the substrates to obtain better films.

METHODS

Growth and Characterization. All samples were grown using a Perkin–Elmer MBE system with a background pressure of $\sim 10^{-9}$ Torr. Boron was supplied by a Knudsen effusion cell filled with the B_2O_3 powder (Alfa Aesar, 99.999% purity), and nitrogen was supplied by introducing ammonia (American Gas Group, 99.9995% purity) through a mass flow controller. XRD spectra were acquired using a Panalytical Empyrean Series 2 system. Secondary electron SEM images and EBSD images were acquired using a FEI NNS450 system. Raman mapping was performed using a HORIBA LabRam system equipped with a 60 mW, 532 nm green laser. Tapping mode AFM images were acquired using a Veeco D5000 AFM system. Bright-field TEM images and SAED patterns were obtained using a FEI Tecnai12 system. XPS spectra were acquired using a Kratos AXIS ULTRA XPS system and deconvoluted using CasaXPS. An STM image was acquired using NaioSTM, a tabletop STM from Nanosurf.

Theoretical Calculations. The adsorption energy was obtained by first-principles DFT calculations using the software package VASP. The projector augmented wave method and the Perdew–Burke–Ernzerhof (PBE) type generalized gradient approximation[64,65] were employed, and spin polarization was included self-consistently. The CI-NEB method was adopted[66] for the calculation of diffusion activation energies. Detailed calculation parameters are available in our previous paper.[55]

Device Fabrication and Characterization. Metal–insulator–metal (MIM) devices were fabricated by depositing metal contacts (Ni) of 100 nm on the as-grown film using e-beam evaporation. Photolithography and etching were performed to form square Ni metal contacts of 50 μm × 50 μm. The Ni substrate was used as a

https://dx.doi.org/10.1021/acsami.0c07201
ACS Appl. Mater. Interfaces 2020, 12, 35318–35327

global bottom contact for all devices. Device characterization was performed on a Signatone probe station connected with an Agilent 4155C semiconductor parameter analyzer.

■ ASSOCIATED CONTENT

Supporting Information

The Supporting Information is available free of charge at https://pubs.acs.org/doi/10.1021/acsami.0c07201.

> Substrate preparation; DFT calculation of the geometric structure of h-BN/Ni (111); characterization of Ni substrates after h-BN growth; multipeak fitting of XPS results (PDF)

■ AUTHOR INFORMATION

Corresponding Author

Jianlin Liu − *Department of Electrical and Computer Engineering, University of California, Riverside, California 92521, United States;* orcid.org/0000-0001-6513-0867; Phone: 1-9518277131; Email: jianlin@ece.ucr.edu; Fax: 1-9518272425

Authors

Yanwei He − *Department of Electrical and Computer Engineering, University of California, Riverside, California 92521, United States*

Hao Tian − *Department of Electrical and Computer Engineering, University of California, Riverside, California 92521, United States;* orcid.org/0000-0001-5893-2319

Protik Das − *Department of Electrical and Computer Engineering, University of California, Riverside, California 92521, United States*

Zhenjun Cui − *Department of Electrical and Computer Engineering, University of California, Riverside, California 92521, United States*

Pedro Pena − *Department of Chemistry, University of California, Riverside, California 92521, United States*

Ivan Chiang − *Department of Electrical and Computer Engineering, University of California, Riverside, California 92521, United States*

Wenhao Shi − *Department of Electrical and Computer Engineering, University of California, Riverside, California 92521, United States*

Long Xu − *Department of Electrical and Computer Engineering, University of California, Riverside, California 92521, United States;* orcid.org/0000-0002-3243-4087

Yuan Li − *Department of Electrical and Computer Engineering, University of California, Riverside, California 92521, United States*

Tianchen Yang − *Department of Electrical and Computer Engineering, University of California, Riverside, California 92521, United States*

Miguel Isarraraz − *Department of Electrical and Computer Engineering, University of California, Riverside, California 92521, United States*

Cengiz S. Ozkan − *Materials Science and Engineering Program and Department of Mechanical Engineering, University of California, Riverside, California 92521, United States;* orcid.org/0000-0001-6751-6851

Mihrimah Ozkan − *Department of Electrical and Computer Engineering, University of California, Riverside, California 92521, United States*

Roger K. Lake − *Department of Electrical and Computer Engineering, University of California, Riverside, California 92521, United States*

Complete contact information is available at: https://pubs.acs.org/10.1021/acsami.0c07201

Notes

The authors declare no competing financial interest.

■ ACKNOWLEDGMENTS

This work was supported by SHINES, an Energy Frontier Research Center (EFRC) funded by the US Department of Energy, The Office of Science, Basic Energy Sciences, under Award #SC0012670. This work used the Extreme Science and Engineering Discovery Environment (XSEDE),[67] which is supported by National Science Foundation Grant no. ACI-1548562 and allocation ID TG-DMR13008.

■ REFERENCES

(1) Liu, C.; Yu, Z.; Neff, D.; Zhamu, A.; Jang, B. Z. Graphene-Based Supercapacitor with an Ultrahigh Energy Density. *Nano Lett.* **2010**, *10*, 4863−4868.

(2) Cui, Y.; Xin, R.; Yu, Z.; Pan, Y.; Ong, Z. Y.; Wei, X.; Wang, J.; Nan, H.; Ni, Z.; Wu, Y.; et al. High-performance Monolayer WS_2 Field-Effect Transistors on High-κ Dielectrics. *Adv. Mater.* **2015**, *27*, 5230−5234.

(3) Liu, W.; Kang, J.; Sarkar, D.; Khatami, Y.; Jena, D.; Banerjee, K. Role of Metal Contacts in Designing High-Performance Monolayer n-Type WSe2 Field Effect Transistors. *Nano Lett.* **2013**, *13*, 1983−1990.

(4) Jing, X.; Panholzer, E.; Song, X.; Grustan-Gutierrez, E.; Hui, F.; Shi, Y.; Benstetter, G.; Illarionov, Y.; Grasser, T.; Lanza, M. Fabrication of Scalable and Ultra Low Power Photodetectors with High Light/Dark Current Ratios Using Polycrystalline Monolayer MoS_2 Sheets. *Nano Energy* **2016**, *30*, 494−502.

(5) Cassabois, G.; Valvin, P.; Gil, B. Hexagonal Boron Nitride Is an Indirect Bandgap Semiconductor. *Nat. Photonics* **2016**, *10*, 262−266.

(6) Hattori, Y.; Taniguchi, T.; Watanabe, K.; Nagashio, K. Layer-by-Layer Dielectric Breakdown of Hexagonal Boron Nitride. *ACS Nano* **2015**, *9*, 916−921.

(7) Jo, I.; Pettes, M. T.; Kim, J.; Watanabe, K.; Taniguchi, T.; Yao, Z.; Shi, L. Thermal Conductivity and Phonon Transport in Suspended Few-Layer Hexagonal Boron Nitride. *Nano Lett.* **2013**, *13*, 550−554.

(8) Kostoglou, N.; Polychronopoulou, K.; Rebholz, C. Thermal and Chemical Stability of Hexagonal Boron Nitride (h-BN) Nanoplatelets. *Vacuum* **2015**, *112*, 42−45.

(9) Lee, G.-H.; Yu, Y.-J.; Cui, X.; Petrone, N.; Lee, C.-H.; Choi, M. S.; Lee, D.-Y.; Lee, C.; Yoo, W. J.; Watanabe, K.; et al. Flexible and Transparent MoS2 Field-Effect Transistors on Hexagonal Boron Nitride-Graphene Heterostructures. *ACS Nano* **2013**, *7*, 7931−7936.

(10) Jang, S. K.; Youn, J.; Song, Y. J.; Lee, S. Synthesis and Characterization of Hexagonal Boron Nitride as a Gate Dielectric. *Sci. Rep.* **2016**, *6*, No. 30449.

(11) Jing, X.; Puglisi, F.; Akinwande, D.; Lanza, M. Chemical Vapor Deposition of Hexagonal Boron Nitride on Metal-Coated Wafers and Transfer-Free Fabrication of Resistive Switching Devices. *2D Mater.* **2019**, *6*, No. 035021.

(12) Pan, C.; Miranda, E.; Villena, M. A.; Xiao, N.; Jing, X.; Xie, X.; Wu, T.; Hui, F.; Shi, Y.; Lanza, M. Model for Multi-Filamentary Conduction in Graphene/Hexagonal-Boron-Nitride/Graphene Based Resistive Switching Devices. *2D Mater.* **2017**, *4*, No. 025099.

(13) Dean, C. R.; Young, A. F.; Meric, I.; Lee, C.; Wang, L.; Sorgenfrei, S.; Watanabe, K.; Taniguchi, T.; Kim, P.; Shepard, K. L.; Hone, J. Boron Nitride Substrates for High-Quality Graphene Electronics. *Nat. Nanotechnol.* **2010**, *5*, 722−726.

(14) Dean, C. R.; Young, A. F.; Cadden-Zimansky, P.; Wang, L.; Ren, H.; Watanabe, K.; Taniguchi, T.; Kim, P.; Hone, J.; Shepard, K. Multicomponent Fractional Quantum Hall Effect in Graphene. *Nat. Phys.* **2011**, *7*, 693−696.
(15) Cui, X.; Lee, G.-H.; Kim, Y. D.; Arefe, G.; Huang, P. Y.; Lee, C.-H.; Chenet, D. A.; Zhang, X.; Wang, L.; Ye, F.; et al. Multi-Terminal Transport Measurements of MoS2 Using a van der Waals Heterostructure Device Platform. *Nat. Nanotechnol.* **2015**, *10*, 534−540.
(16) Murakami, K.; Igari, T.; Mitsuishi, K.; Nagao, M.; Sasaki, M.; Yamada, Y. Highly Monochromatic Electron Emission from Graphene-Hexagonal Boron Nitride-Si Heterostructure. *ACS Appl. Mater. Interfaces* **2020**, *12*, 4061−4067.
(17) Novoselov, K. S.; Geim, A. K.; Morozov, S. V.; Jiang, D.; Zhang, Y.; Dubonos, S. V.; Grigorieva, I. V.; Firsov, A. A. Electric Field Effect in Atomically Thin Carbon Films. *Science* **2004**, *306*, 666−669.
(18) Huang, Y.; Sutter, E.; Shi, N. N.; Zheng, J.; Yang, T.; Englund, D.; Gao, H.-J.; Sutter, P. Reliable Exfoliation of Large-Area High-Quality Flakes of Graphene and Other Two-Dimensional Materials. *ACS Nano* **2015**, *9*, 10612−10620.
(19) Hernandez, Y.; Nicolosi, V.; Lotya, M.; Blighe, F. M.; Sun, Z.; De, S.; McGovern, I.; Holland, B.; Byrne, M.; Gun'Ko, Y. K.; et al. High-Yield Production of Graphene by Liquid-Phase Exfoliation of Graphite. *Nat. Nanotechnol.* **2008**, *3*, 563−568.
(20) Zhao, H.-R.; Ding, J.-H.; Shao, Z.-Z.; Xu, B.-Y.; Zhou, Q.-B.; Yu, H.-B. High-Quality Boron Nitride Nanosheets and Their Bioinspired Thermally Conductive Papers. *ACS Appl. Mater. Interfaces* **2019**, *11*, 37247−37255.
(21) Shi, Y.; Hamsen, C.; Jia, X.; Kim, K. K.; Reina, A.; Hofmann, M.; Hsu, A. L.; Zhang, K.; Li, H.; Juang, Z.-Y. Synthesis of Few-Layer Hexagonal Boron Nitride Thin Film by Chemical Vapor Deposition. *Nano Lett.* **2010**, *10*, 4134−4139.
(22) Ferguson, J.; Weimer, A.; George, S. Atomic Layer Deposition of Boron Nitride Using Sequential Exposures of BCl3 and NH3. *Thin Solid Films* **2002**, *413*, 16−25.
(23) Driver, M. S.; Beatty, J. D.; Olanipekun, O.; Reid, K.; Rath, A.; Voyles, P. M.; Kelber, J. A. Atomic Layer Epitaxy of h-BN (0001) Multilayers on Co (0001) and Molecular Beam Epitaxy Growth of Graphene on h-BN (0001)/Co (0001). *Langmuir* **2016**, *32*, 2601−2607.
(24) Nakhaie, S.; Wofford, J.; Schumann, T.; Jahn, U.; Ramsteiner, M.; Hanke, M.; Lopes, J.; Riechert, H. Synthesis of Atomically Thin Hexagonal Boron Nitride Films on Nickel Foils by Molecular Beam Epitaxy. *Appl. Phys. Lett.* **2015**, *106*, No. 213108.
(25) Zuo, Z.; Xu, Z.; Zheng, R.; Khanaki, A.; Zheng, J.-G.; Liu, J. In-situ Epitaxial Growth of Graphene/h-BN van der Waals Heterostructures by Molecular Beam Epitaxy. *Sci. Rep.* **2015**, *5*, No. 14760.
(26) Vuong, T.; Cassabois, G.; Valvin, P.; Rousseau, E.; Summerfield, A.; Mellor, C.; Cho, Y.; Cheng, T.; Albar, J. D.; Eaves, L.; et al. Deep Ultraviolet Emission in Hexagonal Boron Nitride Grown by High-Temperature Molecular Beam Epitaxy. *2D Mater.* **2017**, *4*, No. 021023.
(27) Cho, Y.-J.; Summerfield, A.; Davies, A.; Cheng, T. S.; Smith, E. F.; Mellor, C. J.; Khlobystov, A. N.; Foxon, C. T.; Eaves, L.; Beton, P. H.; Novikov, S. V. Hexagonal Boron Nitride Tunnel Barriers Grown on Graphite by High Temperature Molecular Beam Epitaxy. *Sci. Rep.* **2016**, *6*, No. 34474.
(28) Zheng, R.; Khanaki, A.; Tian, H.; He, Y.; Cui, Y.; Xu, Z.; Liu, J. Precipitation Growth of Graphene under Exfoliated Hexagonal Boron Nitride to Form Heterostructures on Cobalt Substrate by Molecular Beam Epitaxy. *Appl. Phys. Lett.* **2017**, *111*, No. 011903.
(29) Pierucci, D.; Zribi, J.; Henck, H.; Chaste, J.; Silly, M. G.; Bertran, F.; Le Fevre, P.; Gil, B.; Summerfield, A.; Beton, P. H.; Novikov, S. V.; et al. Van der Waals Epitaxy of Two-Dimensional Single-Layer H-BN on Graphite by Molecular Beam Epitaxy: Electronic Properties and Band Structure. *Appl. Phys. Lett.* **2018**, *112*, No. 253102.
(30) Cho, Y. J.; Summerfield, A.; Davies, A.; Cheng, T. S.; Smith, E. F.; Mellor, C. J.; Khlobystov, A. N.; Foxon, C. T.; Eaves, L.; Beton, P. H.; Novikov, S. V. Hexagonal Boron Nitride Tunnel Barriers Grown on Graphite by High Temperature Molecular Beam Epitaxy. *Sci. Rep.* **2016**, *6*, No. 34474.
(31) Elias, C.; Valvin, P.; Pelini, T.; Summerfield, A.; Mellor, C. J.; Cheng, T. S.; Eaves, L.; Foxon, C. T.; Beton, P. H.; Novikov, S. V.; Gil, B.; Cassabois, G. Direct Band-Gap Crossover in Epitaxial Monolayer Boron Nitride. *Nat. Commun.* **2019**, *10*, No. 2639.
(32) Caneva, S.; Weatherup, R. S.; Bayer, B. C.; Blume, R.; Cabrero-Vilatela, A.; Braeuninger-Weimer, P.; Martin, M.-B.; Wang, R.; Baehtz, C.; Schloegl, R.; Meyer, J. C.; Hofmann, S. Controlling Catalyst Bulk Reservoir Effects for Monolayer Hexagonal Boron Nitride CVD. *Nano Lett.* **2016**, *16*, 1250−1261.
(33) Sharma, K. P.; Sharma, S.; Sharma, A. K.; Jaisi, B. P.; Kalita, G.; Tanemura, M. Edge Controlled Growth of Hexagonal Boron Nitride Crystals on Copper Foil by Atmospheric Pressure Chemical Vapor Deposition. *CrystEngComm* **2018**, *20*, 550−555.
(34) Wood, G. E.; Marsden, A. J.; Mudd, J. J.; Walker, M.; Asensio, M.; Avila, J.; Chen, K.; Bell, G. R.; Wilson, N. R. Wan der Waals Epitaxy of Monolayer Hexagonal Boron Nitride on Copper Foil: Growth, Crystallography and Electronic Band Structure. *2D Mater.* **2015**, *2*, No. 025003.
(35) Khanaki, A.; Tian, H.; Xu, Z.; Zheng, R.; He, Y.; Cui, Z.; Yang, J.; Liu, J. Effect of High Carbon Incorporation in Co Substrates on the Epitaxy of Hexagonal Boron Nitride/Graphene Heterostructures. *Nanotechnology* **2018**, *29*, No. 035602.
(36) Xu, Z.; Tian, H.; Khanaki, A.; Zheng, R.; Suja, M.; Liu, J. Large-Area Growth of Multi-Layer Hexagonal Boron Nitride on Polished Cobalt Foils by Plasma-Assisted Molecular Beam Epitaxy. *Sci. Rep.* **2017**, *7*, No. 43100.
(37) He, Y.; Tian, H.; Khanaki, A.; Shi, W.; Tran, J.; Cui, Z.; Wei, P.; Liu, J. Large-Area Adlayer-Free Single-Layer h-BN Film Achieved by Controlling Intercalation Growth. *Appl. Surf. Sci.* **2019**, *498*, No. 143851.
(38) Kim, S. M.; Hsu, A.; Park, M. H.; Chae, S. H.; Yun, S. J.; Lee, J. S.; Cho, D.-H.; Fang, W.; Lee, C.; Palacios, T.; et al. Synthesis of Large-area Multilayer Hexagonal Boron Nitride for High Material Performance. *Nat. Commun.* **2015**, *6*, No. 8662.
(39) Uchida, Y.; Nakandakari, S.; Kawahara, K.; Yamasaki, S.; Mitsuhara, M.; Ago, H. Controlled Growth of Large-Area Uniform Multilayer Hexagonal Boron Nitride as an Effective 2D Substrate. *ACS Nano* **2018**, *12*, 6236−6244.
(40) Caneva, S.; Weatherup, R. S.; Bayer, B. C.; Brennan, B.; Spencer, S. J.; Mingard, K.; Cabrero-Vilatela, A.; Baehtz, C.; Pollard, A. J.; Hofmann, S. Nucleation Control for Large, Single Crystalline Domains of Monolayer Hexagonal Boron Nitride via Si-Doped Fe Catalysts. *Nano Lett.* **2015**, *15*, 1867−1875.
(41) Zhuang, P.; Lin, W.; Xu, B.; Cai, W. Oxygen-Assisted Synthesis of Hexagonal Boron Nitride Films for Graphene Transistors. *Appl. Phys. Lett.* **2017**, *111*, No. 203103.
(42) Babenko, V.; Fan, Y.; Veigang-Radulescu, V.-P.; Brennan, B.; Pollard, A. J.; Burton, O.; Alexander-Webber, J. A.; Weatherup, R. S.; Canto, B.; Otto, M.; Neumaier, D.; Hofmann, S. Oxidising and Carburising Catalyst Conditioning for the Controlled Growth and Transfer of Large Crystal Monolayer Hexagonal Boron Nitride. *2D Mater.* **2020**, *7*, No. 024005.
(43) Tian, H.; Khanaki, A.; Das, P.; Zheng, R.; Cui, Z.; He, Y.; Shi, W.; Xu, Z.; Lake, R.; Liu, J. Role of Carbon Interstitials in Transition Metal Substrates on Controllable Synthesis of High-Quality Large-Area Two-Dimensional Hexagonal Boron Nitride Layers. *Nano Lett.* **2018**, *18*, 3352−3361.
(44) Khan, M. H.; Huang, Z.; Xiao, F.; Casillas, G.; Chen, Z.; Molino, P. J.; Liu, H. K. Synthesis of Large and few atomic layers of hexagonal boron nitride on melted copper. *Sci. Rep.* **2015**, *5*, No. 7743.
(45) Li, X.; Li, Y.; Wang, Q.; Yin, J.; Li, J.; Yu, J.; Guo, W. Oxygen-Suppressed Selective Growth of Monolayer Hexagonal Boron Nitride on Copper Twin Crystals. *Nano Res.* **2017**, *10*, 826−833.

(46) Cho, H.; Park, S.; Won, D.-I.; Kang, S. O.; Pyo, S.-S.; Kim, D.-I.; Kim, S. M.; Kim, H. C.; Kim, M. J. Growth Kinetics of White Graphene (h-BN) on a Planarised Ni Foil Surface. *Sci. Rep.* **2015**, *5*, No. 11985.
(47) Kadhim, N. J.; Mukherjee, D. Rate-Temperature Relation for MBE Growth of GaAs Layers. *Int. J. Electron.* **1990**, *69*, 641−645.
(48) Shaw, D. W. Influence of Substrate Temperature on GaAs Epitaxial Deposition Rates. *J. Electrochem. Soc.* **1968**, *115*, 405−408.
(49) Schneider, C. A.; Rasband, W. S.; Eliceiri, K. W. NIH Image to ImageJ: 25 Years of Image Analysis. *Nat. Methods* **2012**, *9*, 671−675.
(50) Auwärter, W.; Muntwiler, M.; Osterwalder, J.; Greber, T. Defect Lines and Two-Domain Structure of Hexagonal Boron Nitride Films on Ni (1 1 1). *Surf. Sci.* **2003**, *545*, L735−L740.
(51) Yang, Y.; Fu, Q.; Li, H.; Wei, M.; Xiao, J.; Wei, W.; Bao, X. Creating a Nanospace under an h-BN Cover for Adlayer Growth on Nickel (111). *ACS Nano* **2015**, *9*, 11589−11598.
(52) Sun, X.; Pratt, A.; Li, Z.; Ohtomo, M.; Sakai, S.; Yamauchi, Y. The Adsorption of h-BN Monolayer on the Ni (111) Surface Studied by Density Functional Theory Calculations with a Semiempirical Long-Range Dispersion Correction. *J. Appl. Phys.* **2014**, *115*, No. 17C117.
(53) Huda, M.; Kleinman, L. H-BN Monolayer Adsorption on the Ni (111) Surface: A Density Functional Study. *Phys. Rev. B: Condens. Matter Mater. Phys.* **2006**, *74*, No. 075418.
(54) Grad, G.; Blaha, P.; Schwarz, K.; Auwärter, W.; Greber, T. Density Functional Theory Investigation of the Geometric and Spintronic Structure of h-BN/Ni (111) in View of Photoemission and STM Experiments. *Phys. Rev. B: Condens. Matter Mater. Phys.* **2003**, *68*, No. 085404.
(55) Tian, H.; He, Y.; Das, P.; Cui, Z.; Shi, W.; Khanaki, A.; Lake, R. K.; Liu, J. Growth Dynamics of Millimeter-Sized Single-Crystal Hexagonal Boron Nitride Monolayers on Secondary Recrystallized Ni (100) Substrates. *Adv. Mater. Interfaces* **2019**, *6*, No. 1901198.
(56) Yin, S.; Xu, B.; Zhou, X.; Au, C. A Mini-Review on Ammonia Decomposition Catalysts for On-Site Generation of Hydrogen for Fuel Cell Applications. *Appl. Catal., A* **2004**, *277*, 1−9.
(57) Arenal, R.; Ferrari, A.; Reich, S.; Wirtz, L.; Mevellec, J.-Y.; Lefrant, S.; Rubio, A.; Loiseau, A. Raman Spectroscopy of Single-Wall Boron Nitride Nanotubes. *Nano Lett.* **2006**, *6*, 1812−1816.
(58) Simmons, J. G. Generalized Formula for the Electric Tunnel Effect Between Similar Electrodes Separated by a Thin Insulating Film. *J. Appl. Phys.* **1963**, *34*, 1793−1803.
(59) Jiang, L.; Shi, Y.; Hui, F.; Tang, K.; Wu, Q.; Pan, C.; Jing, X.; Uppal, H.; Palumbo, F.; Lu, G.; et al. Dielectric Breakdown in Chemical Vapor Deposited Hexagonal Boron Nitride. *ACS Appl. Mater. Interfaces* **2017**, *9*, 39758−39770.
(60) Simmons, J. G. Generalized Thermal J-V Characteristic for the Electric Tunnel Effect. *J. Appl. Phys.* **1964**, *35*, 2655−2658.
(61) Cui, Z.; He, Y.; Tian, H.; Khanaki, A.; Xu, L.; Shi, W.; Liu, J. Study of Direct Tunneling and Dielectric Breakdown in Molecular Beam Epitaxial Hexagonal Boron Nitride Monolayers Using Metal-Insulator-Metal Devices. *ACS Appl. Electron. Mater.* **2020**, *2*, 747−755.
(62) Lee, G.-H.; Yu, Y.-J.; Lee, C.; Dean, C.; Shepard, K. L.; Kim, P.; Hone, J. Electron Tunneling through Atomically Flat and Ultrathin Hexagonal Boron Nitride. *Appl. Phys. Lett.* **2011**, *99*, No. 243114.
(63) Dodson, B. *Weibull Analysis*; Asq Press, 1994.
(64) Perdew, J. P.; Burke, K.; Ernzerhof, M. Generalized Gradient Approximation Made Simple. *Phys. Rev. Lett.* **1996**, *77*, 3865−3868.
(65) Ernzerhof, M.; Scuseria, G. E. Assessment of the Perdew−Burke−Ernzerhof Exchange-Correlation Functional. *J. Chem. Phys.* **1999**, *110*, 5029−5036.
(66) Henkelman, G.; Uberuaga, B. P.; Jónsson, H. A Climbing Image Nudged Elastic Band Method for Finding Saddle Points and Minimum Energy Paths. *J. Chem. Phys.* **2000**, *113*, 9901−9904.
(67) Towns, J.; Cockerill, T.; Dahan, M.; Foster, I.; Gaither, K.; Grimshaw, A.; Hazlewood, V.; Lathrop, S.; Lifka, D.; Peterson, G. D.; et al. XSEDE: Accelerating Scientific Discovery. *Comput. Sci. Eng.* **2014**, *16*, 62−74.

https://dx.doi.org/10.1021/acsami.0c07201
ACS Appl. Mater. Interfaces 2020, 12, 35318−35327